# Controlling Polymer Microfiber Structure by Micro Solution Blow Spinning

*Eddie Hofmann, Martin Dulle, Xiaojian Liao, Andreas Greiner, and Stephan Förster\**

Recent progress in microfluidic technology allows fabricating microfluidic devices to produce liquid microjets with unprecedented control of the jet diameter and velocity. Here it is demonstrated that microfluidic devices based on the gas dynamic virtual nozzle principle can be excellently used for micro solution blow spinning to continuously fabricate microfibers with excellent control of the fiber diameter and the internal crystalline alignment that determines the mechanical properties. Fiber spinning experiments with small- and wide-angle X-ray scattering are combined to directly relate the macroscopic spinning conditions to the bulk and molecular structure of the resulting fibers. The elongational rate is shown as the relevant parameter that transduces the nozzle flow conditions to the local macromolecular structure and orientation, and thus the mechanical properties of the resulting fiber. It is observed that the spinning process results in very uniform microfibers with a well-defined shish–kebab crystal structure, which evolves into an extended chain crystal structure upon plastic deformation. Thus, the presented microfluidic spinning methodology has great implications for a precisely controlled production of microfibers using miniaturized spinning devices.

## 1. Introduction

Solution blow spinning (SBS) was introduced by Medeiros et al. in the year 2009.[1] By combining conceptual elements from dry spinning, melt blowing, and electrospinning, SBS produces micro-scale fibers in a simple one-step process using a small,

E. Hofmann, Dr. M. Dulle, Prof. S. Förster
Department of Physical Chemistry I
University of Bayreuth
95440 Bayreuth, Germany
E-mail: s.foerster@fz-juelich.de
E. Hofmann, Dr. M. Dulle, Prof. S. Förster
Jülich Centre for Neutron Science (JCNS-1/ICS-1)
Forschungszentrum Jülich GmbH
52425 Jülich, Germany
X. Liao, Prof. A. Greiner
Department of Macromolecular Chemistry II
University of Bayreuth
95440 Bayreuth, Germany

The ORCID identification number(s) for the author(s) of this article can be found under https://doi.org/10.1002/macp.201900453.

compact, and portable spinning device.[2,3] In the device, the polymer spinning dope solution is surrounded by a high-velocity air flow and thereby focused into a thin liquid jet. After the evaporation of the solvent, the resulting fiber can either be spooled or collected as a non-woven fabric.[1] The produced nanofiber mats and scaffolds are of great interest for biomedical applications like drug delivery and tissue engineering,[4–6] with the possibility of direct application onto wounds or tissues.[1,7]

Previous investigations on SBS have focused on empirical and qualitative relationships between specific process parameters (gas pressure, flow rate), solution parameters (solvent, polymer solution concentration, molecular weight), and fiber diameter.[1,3,8–11] In a more detailed study, X-ray diffraction was employed to determine crystallinity, *d*-spacing, and crystallite size of SBS-produced fibers in comparison to electrospun fibers and casted films.[7] However, a complete and quantitative relation between the main blow spinning parameters and the structure of the resulting fiber is still lacking.

In this study, we use a lithographically produced microfluidic nozzle device to produce fibers at controlled spinning conditions. The design of the microfluidic device was introduced recently.[12]

It allows controlling the velocity and diameter of the exiting liquid jet with high precision. Here we demonstrate using continuous microfluidic solution blow spinning (μSBS) together with small- and wide-angle X-ray scattering (SAXS, WAXS) that this microfluidic device enables unique quantitative control of the spinning conditions to suitably tailor the microfiber diameter and its internal macromolecular alignment. It thus has great implications for a quantitatively controlled production of microfibers using highly miniaturized spinning devices.

## 2. Experimental Section

### 2.1. Fabrication of Microfluidic Devices

The nozzle devices for μSBS were produced using standard photolithography and soft lithography techniques. The complete procedure was described in detail in a previous publication.[12] By using photolithography, a microstructured master was produced and afterward casted with poly(dimethylsiloxane) (PDMS; Sylgard 184 kit, Dow Corning Corp.). Two individually

**ADVANCED
SCIENCE NEWS**

www.advancedsciencenews.com

**Macromolecular
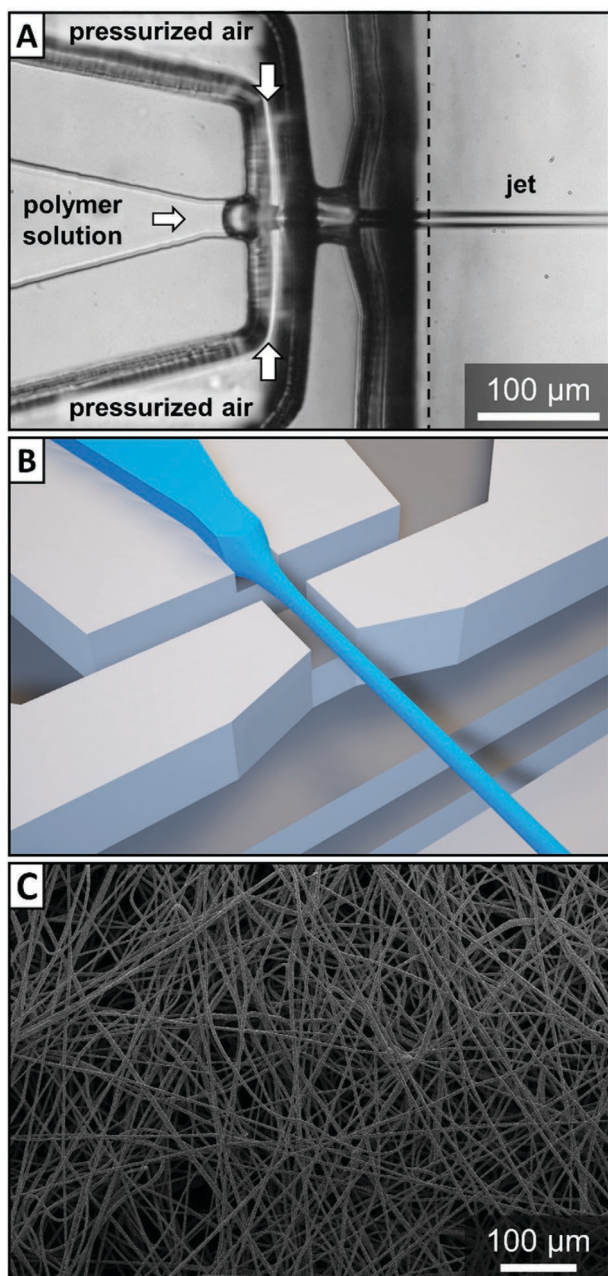Chemistry and Physics**

www.mcp-journal.de

**Figure 1.** A) Microscopic image and B) 3D model of the nozzle which is used to produce a liquid jet of polymer solution. Due to different focal planes image (A) is composed of two photos indicated by a dashed line. To reveal the 3D architecture of the microfluidic device, just the lower half of the device is shown in image (B). C) SEM image of the produced fibers.

structured PDMS halves were combined to create a 3D-focusing nozzle device. The nozzle design is schematically shown in **Figure 1**.

### 2.2. Microfluidic Solution Blow Spinning and Sample Collection

For the spinning process, a 20% w/w polymer solution of 3M Dyneon THV 221GZ (3M Deutschland GmbH) in acetone was used ($\eta$ = 1.0 Pa s). This concentration was sufficiently high to achieve stable fiber spinning conditions. The macromolecular structure and thermal properties of the polymer have already been characterized.[13,14] Accordingly, the polymer has a chemical composition of 43.8 mol% tetrafluoroethylene (TFE), 46.0 mol% vinylidene fluoride (VDF), and 10.2 mol% hexafluoropropylene (HFP), a molecular weight of 4100 g mol$^{-1}$, and a broad melting temperature range between 365 and 400 K. The spinning solution was filled into a glass syringe (1.0 mL, Gastight 1000 Series, Hamilton Company), which was connected via LDPE tubing (0.38 mm I.D., 1.09 mm O.D., Science Commodities Inc.) to the microfluidic nozzle device. Precise pumping of the spinning solution at constant flow rates between 0.5 and 4.0 mL h$^{-1}$ was ensured by using a syringe pump (neMESYS 290N, Cetoni GmbH). Inside the nozzle, the spinning solution was focused by a constant air flow, which was adjusted by a pressure controller with a manometer to a value between 0.5 and 3.0 bar. The fiber spinning was conducted at ambient conditions of 23 °C room temperature and a relative humidity in the range of 45–55%.

Fiber samples were collected on a cork spool driven by a rotary tool (Proxxon GmbH). The distance between nozzle and spool as well as the rotational speed were continuously adjustable. The drawing speed could be calculated by using the diameter of the cork spool (61.8 mm). The advantage of the cork material was that the fibers did not adhere to it and could be bundled easily into a strand of fibers. Several representative images, taken by a scanning electron microscope (SEM; JSM-6510LV, JEOL GmbH), were statistically analyzed using ImageJ software (National Institutes of Health) to determine the quadratic mean and the standard deviation of the fiber diameter for each sample.

### 2.3. SAXS Measurement and Tensile Testing

The SAXS measurements were performed in-house at a GANESHA (SAXSLAB) instrument equipped with a micro-focusing rotating anode (copper anode, $\lambda$ = 0.154 nm, MicroMax 007 HF, Rigaku) and a Pilatus 300K detector (DECTRIS). The fiber samples were measured at a sample–detector distance of 0.44 m.

Using a custom-built tensile apparatus, fiber samples were manually stretched to a certain strain value and fixed for SAXS measurements at constant strains of 50%, 100%, 150%, 200%, 300%, 400%, and 600%. The tensile tests of strands of fibers were performed by using a universal testing machine Zwick/Roell Z0.5 (BT1-FR0.5TN.D14, Zwick GmbH & Co. KG) equipped with a load cell KAF-TC (nominal load: 200 N, Zwick GmbH & Co. KG).

## 3. Results

### 3.1. Principle of Microfluidic Solution Blow Spinning

In this study, we investigated the correlation between the spinning parameters and the microstructure of THV fibers obtained from SBS. THV is a fluoroplastic terpolymer, poly(TFE-co-HFP-co-VDF) composed of TFE, HFP, and VDF. µSBS utilizes the

gas dynamic virtual nozzle (GDVN) principle[15] to produce micron-sized fibers from a polymer solution in a continuous and stable process. Inside the nozzle of a microfluidic device a steady flow of pressurized air focuses the polymer solution from orthogonal directions so that a fine liquid jet is produced (Figure 1A). A complete 3D focusing is achieved by using a multi-layer architecture of the PDMS device as schematically shown in Figure 1B, where the upper half of the microfluidic device is masked out for the image. The pressurized air approaches from all sides and encase the liquid jet entirely. The fabrication of the microfluidic device and the spinning process is described in detail in a previous publication.[12] An SEM image of the spun THV fibers is shown in Figure 1C.

### 3.2. Fiber Spinning Hydrodynamics

With the developed microfluidic nozzle device, it is possible to uniquely control all parameters that define the molecular and macroscopic fiber properties. The most important parameters are the velocities $v$ and diameters $d$ of i) the solution inside the nozzle, ii) the liquid jet, and iii) the emerging fiber before and iv) after drawing. In the following, we outline the basic equations that relate the velocities to the jet and fiber diameters.

For incompressible fluids, flow volume conservation relates velocities $v$ and diameters $d$ to the volumetric flow rate $Q$ as

$$Q = A \times v = \frac{d^2 \pi \times v}{4} \tag{1}$$

where $A$ is the cross-sectional area, which is assumed to be circular with a diameter $d$. In the experiment the three variable control parameters that determine jet and fiber formation are the volumetric flow rate $Q$, the pressure difference $\Delta p$, and the spooling rotational velocity $v_s$.

We consider four positions that are relevant for jet and fiber formation: i) the flowing polymer solution in the microfluidic channel just before the channel exit with flow velocity $v_n$ and channel diameter $d_n$, ii) the free fluid jet after exiting the nozzle with a jet velocity $v_j$ and a jet diameter $d_j$, iii) the free fiber after evaporation of the solvent with a fiber velocity $v_f$ and a diameter $d_f$, and iv) the spooled and thereby stretched fiber with a velocity $v_s$ and a final diameter $d_s$.

i. The flow velocity $v_n$ of the polymer solution in the microfluidic channel exit can be calculated from the channel dimensions as

$$v_n = \frac{Q}{w_n \times h_n} \tag{2}$$

where $w_n$ is the width and $h_n$ the height of the channel. Their values are fixed for a given microfluidic device. In the present example the values are $w_n = 34.6\ \mu m$ and $h_n = 30.0\ \mu m$ (**Table 1**).

ii. The velocity of the free jet is determined by Bernoulli's law as[12]

$$v_j = f_j \times \sqrt{\frac{2 \times \Delta p}{\rho_0}} \tag{3}$$

**Table 1.** Relations between jet and fiber diameters to the flow velocity in each of the four sections relevant for fiber formation.

| Section | Diameter | Velocity | Remarks |
|---|---|---|---|
| Nozzle exit | $w_n = 34.6\ \mu m$ $h_n = 30.0\ \mu m$ | $v_n = \dfrac{Q}{w_n \times h_n}$ | Diameter set by nozzle design |
| Free jet | $d_j = \sqrt{\dfrac{4 \times Q}{\pi \times v_j}}$ | $v_j = f_j \times \sqrt{\dfrac{2\Delta p}{\rho_0}}$ | Velocity set by pressure |
| Free fiber | $d_f = \sqrt{\phi_T} \times d_j$ | $v_f = v_j$ | Assuming complete evaporation |
| Spooled fiber | $d_s = \sqrt{\dfrac{4 \times \phi_T \times Q}{\pi \times v_s}}$ | $v_s = d_{spool} \pi \times v_{spool}$ | Velocity set by spool |

where $\rho_0$ is the density of the solution and $\Delta p$ the pressure difference. In our setup, the pressure difference could not be measured at the nozzle directly. Experimentally, by using high speed cameras to measure the jet velocity,[12] we found that the free jet velocity is lower due to pressure losses in the tubing, internal friction in the microfluidic device, and viscous dissipation during jet formation, which all reduce the jet velocity. Yet, we found that for a given microfluidic device there is a constant proportionality factor $f_j$ for all pressure differences $\Delta p$, which in the present case has a value of $f_j = 0.29$. The jet diameter can then be calculated from Equation (1) as

$$d_j = \left( \frac{8 \times \rho_0}{\pi^2 \times f_j^2 \times \Delta p} \right)^{1/4} \cdot Q^{1/2} \tag{4}$$

iii. The volumetric flow rate $Q^*$ after evaporation of the solvent is given by the volume fraction of the polymer in the polymer solution

$$Q^* = \phi_T \times Q \tag{5}$$

This leads to a reduction of the diameter of the free fiber $d_f$

$$d_f = \sqrt{\phi_T} \times d_j \tag{6}$$

iv. The spool accelerates the fiber to the new velocity $v_s$, which results in a final diameter of the spooled fiber

$$d_s = \sqrt{\frac{4 \times Q^*}{\pi \times v_s}} \tag{7}$$

where the velocity $v_s$ is given by the radius and rotation speed of the spool, that is

$$v_s = d_{spool} \pi \times v_{spool} \tag{8}$$

where $d_{spool}$ is the diameter of the spool and $v_{spool}$ the rotational frequency (cycles per second). The relevant equations are summarized in Table 1.

**1900453 (3 of 9)**

**ADVANCED
SCIENCE NEWS**

www.advancedsciencenews.com

**Macromolecular
Chemistry and Physics**

www.mcp-journal.de

The factor that greatly affects the molecular orientation and the resulting macroscopic fiber properties is the extensional rate

$$\dot{\varepsilon} = \frac{\Delta v}{\Delta x} = \frac{v_s - v_j}{\Delta x} \tag{9}$$

which influences crystallization and crystal orientational order. $\Delta x$ is the distance over which the emerging, mechanically still susceptible fiber is accelerated, which corresponds to the distance over which solvent evaporates and a solid fiber is formed. It can be calculated as

$$\Delta x = \left(\frac{v_s + v_j}{2}\right) \times t_{\text{evap}} \tag{10}$$

where $t_{\text{evap}}$ is the evaporation time. For spherical droplets it is given by

$$t_{\text{evap}} = \frac{d_j^2}{c} \tag{11}$$

where $c$ is a constant given by the evaporation rate of the solvent as (Supporting Information)

$$c = \frac{8 \times M \times D_v \times \Delta p}{\rho \times R \times T} \approx 8.8 \times 10^{-8} \frac{m^2}{s} \tag{12}$$

where $M$ is the molecular weight of the solvent (acetone: $M = 58.1$ g mol$^{-1}$), $\rho$ is the density of the solvent (acetone: $\rho = 0.784$ g mL$^{-1}$), $R$ is the gas constant ($R = 8.314$ J K$^{-1}$ mol$^{-1}$), $T$ is the temperature ($T = 298$ K), and $D_v$ is the diffusivity of the solvent vapor (acetone: $D_v = 1.24 \times 10^{-5}$ m$^2$ s$^{-1}$). This results in a constant $c \approx 8.8 \times 10^{-8}$ m$^2$ s$^{-1}$. For cylindrical jets we expect the constant to be smaller, yet still of the same order of magnitude. Thus, for jet diameters in the range of a few micrometers evaporation times are in the millisecond range and with jet velocities in the range of up to 10 m s$^{-1}$, the orientational distance $\Delta x$ is of the order of tens to hundreds of micrometers and therefore in a relevant range for the experiments.

In terms of the control parameters that are varied in the experiment ($Q$, $\Delta p$, $v_{\text{spool}}$) the extensional rate according to Equations ((9)–(12)) is given by

$$\dot{\varepsilon} = \frac{\Delta v}{\Delta x} = \frac{v_s - v_j}{\left(\frac{v_s + v_j}{2}\right) \times \frac{d_j^2}{c}} \tag{13}$$

Taking into account the proportionalities $d_j^2 \propto \dfrac{Q}{\sqrt{\Delta p}}$ (Equation (4)) and $v_j \propto \sqrt{\Delta p}$ (Equation (2)), we obtain the relation

$$\dot{\varepsilon} \propto \frac{v_s - v_j}{v_s + v_j} \times \frac{v_j}{Q} \tag{14}$$

which will be considered in the experiments. It shows that for large $v_s/v_j$ ratios and small jet diameters the extensional rates are large. As shown in the Supporting Information, from Equation (14) follows an optimal ratio $(v_s/v_j)_{\max} = r^* = (\sqrt{2} - 1)^{-1} \approx 2.4$, for which

the extensional rate $\dot{\varepsilon}$ has a maximum. We expect that under this condition macromolecular chains will align well along the fiber axis, which should lead to high values of the orientational order parameter of the resulting polymer fiber.

### 3.3. Small-Angle X-ray Scattering

SAXS was used to study the influence of the spinning parameters on the microstructure of the THV fiber. For the measurements, the fibers were assembled into a filament yarn and were aligned vertically with respect to the X-ray beam. We observe that the obtained 2D scattering patterns show two distinct features,[16] an oval-shaped pattern along the equator, and two diffuse reflections along the meridian, as can be seen in **Figure 2**A.

The equatorial pattern arises from cylindrical or primary fibril structures, which are aligned along the fiber axis. The meridional reflexes originate from stacks of lamellar disks, which are orientated perpendicular to the fiber axis according to the well-known shish–kebab model. The dimensions and orientation of the cylinders and disks are determined by simulating 2D scattering patterns that match the measured 2D SAXS patterns. For the calculation of the simulated scattering patterns the freely available software *Scatter* was used.[17,18]

The proposed model for the semicrystalline polymer is a shish–kebab structure as schematically shown in Figure 2C.[19] The scattering patterns for the shish–kebab structure were calculated by assuming a model consisting of thin cylinders, representing the shishs which are oriented in fiber direction, and stacks of disks representing the kebabs. The scattering intensity is then calculated as the sum of the contribution from the cylinders and from the disk stacks as

$$I(\mathbf{q}) = (\Delta b)^2 \, \rho_N (\phi_C F_C^2(\mathbf{q}) + \phi_D F_D^2(\mathbf{q}) S(\mathbf{q})) \tag{15}$$

where $\Delta b$ is the scattering length difference between the crystalline and the amorphous phase, $F_C(\mathbf{q})$ is the scattering amplitude of the cylinders, $F_D(\mathbf{q})$ is the scattering amplitude of the disks, $\varphi_C$ and $\varphi_D$ are the volume fractions of the cylinders and disks, $\rho_N = N/V$ is the number density of the particles, $S(\mathbf{q})$ is the lattice factor describing the spatial distribution of the disks, and $\mathbf{q}$ is the scattering vector.

The scattering amplitude $F_C(\mathbf{q}, \mathbf{l}_C, \mathbf{r}_C)$ for cylindrical particles of cross-sectional radius $r_C$ and length $l_C$ can be factorized into[18]

$$F_C(\mathbf{q}, \mathbf{l}_C, \mathbf{r}_C) = F_{C\|}(\mathbf{q}, \mathbf{l}_C) \cdot F_{C\perp}(\mathbf{q}, \mathbf{r}_C) \tag{16}$$

where $F_{C\|}(\mathbf{q}, \mathbf{l}_C)$ is the longitudinal contribution parallel to the cylinder axis, and $F_{C\perp}(\mathbf{q}, \mathbf{r}_C)$ is the contribution from the cross-section of the cylinder. $\mathbf{l}_C = l_C \cdot \mathbf{I}_\|$ is a vector with length $l_C$ and a direction given by the unit vector parallel to the cylinder axis $\mathbf{I}_\|$. $\mathbf{r}_C = r_C \cdot \mathbf{I}_\perp$ is a vector with length $r_C$ and a direction given by the unit vector perpendicular to the cylinder axis $\mathbf{I}_\perp$. The directions are shown in **Figure 3**. The longitudinal and cross-sectional contributions for cylinders are given by

$$F_{C\|}(\mathbf{q}, \mathbf{l}_C) = \frac{\sin(\mathbf{q} \cdot \mathbf{l}_C/2)}{\mathbf{q} \cdot \mathbf{l}_C/2} \tag{17}$$
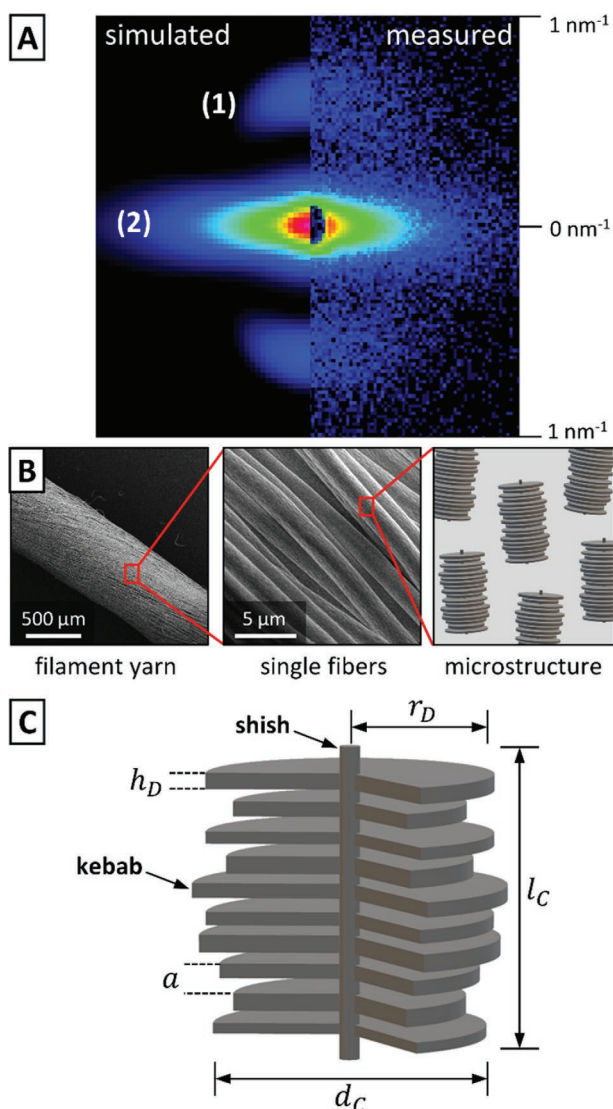
**ADVANCED**
**SCIENCE NEWS**
www.advancedsciencenews.com

**Macromolecular**
**Chemistry and Physics**
www.mcp-journal.de

**Figure 2.** A) Simulated and measured 2D SAXS pattern for THV fibers ($Q = 1$ mL h$^{-1}$, $v_s = 7.7$ m s$^{-1}$, $\Delta p = 2.0$ bar, $d_s = 8$ cm); 1) meridional reflection due to lamellar disks perpendicular to fiber axis and 2) equatorial scattering due to cylindrical structure in fiber direction. The maximum scattering vector is $q_{max} = 1.0$ nm$^{-1}$. B) The shish–kebab model is proposed as morphology of the semicrystalline THV polymer fibers. C) Designation of the structural parameters for the shish–kebab model, which are described in Table S1, Supporting Information.
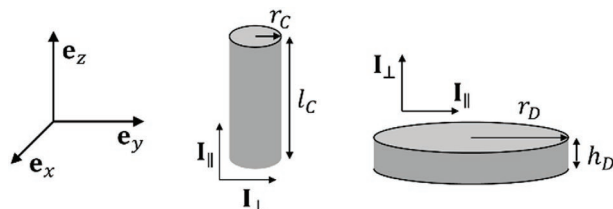


**Figure 3.** Different shapes used for SAXS pattern calculation together with definition of directions for cylinders and disks to calculate the longitudinal and cross-sectional form factors.

$$F_{C\perp}(\mathbf{q}, \mathbf{r}_C) = \frac{2 \cdot J_1(\mathbf{q} \cdot \mathbf{r}_C)}{\mathbf{q} \cdot \mathbf{r}_C} \tag{18}$$

where $J_1(z)$ is the Bessel function of the first kind.

The structure of disks can be described by their lateral radius $r_D$ and the thickness $h_D$ as shown in Figure 3. The longitudinal and cross-sectional contributions for the disks are given by

$$F_D(\mathbf{q}, \mathbf{h}_D, \mathbf{r}_D) = F_{D\parallel}(\mathbf{q}, \mathbf{r}_D) \cdot F_{D\perp}(\mathbf{q}, \mathbf{h}_D) \tag{19}$$

where $F_{D\parallel}(\mathbf{q}, \mathbf{r}_D)$ is now the contribution in the lateral direction and $F_{D\perp}(\mathbf{q}, \mathbf{h}_D)$ is the contribution from the cross-section of the disk. The normal and cross-sectional contributions for disks are

$$F_{D\parallel}(\mathbf{q}, \mathbf{r}_D) = \frac{2 \cdot J_1(\mathbf{q} \cdot \mathbf{r}_D)}{\mathbf{q} \cdot \mathbf{r}_D} \tag{20}$$

$$F_{D\perp}(\mathbf{q}, \mathbf{h}_D) = \frac{\sin(\mathbf{q} \cdot \mathbf{h}_D/2)}{\mathbf{q} \cdot \mathbf{h}_D/2} \tag{21}$$

The structure factor is given by

$$S(\mathbf{q}) = 1 + \beta(\mathbf{q})(Z(\mathbf{q}) - 1)G(\mathbf{q}) \tag{22}$$

where $\beta(\mathbf{q}) = \langle F(\mathbf{q}) \rangle^2 / \langle F^2(\mathbf{q}) \rangle$, $G(\mathbf{q})$ is the Debye–Waller factor, and $Z(\mathbf{q})$ is the lattice factor. For a simple 1D periodic stacking of disks, the lattice factor is given by

$$Z(\mathbf{q}, \mathbf{g}_h) = \frac{2\pi}{a} \sum_{h=1}^{\infty} L_h(\mathbf{q}, \mathbf{g}_h) \tag{23}$$

where $a$ is the repeat distance of the disk stack, $h$ the Miller index, and $\mathbf{g}_h = \frac{2\pi}{a} \mathbf{a}^*$, where $\mathbf{a}^*$ is the reciprocal lattice vector in the stack direction.

For the calculation of the scattering patterns the form factors were averaged over the distribution of lengths $l_C$ and radii $r_C$ the for the cylinders, and over the distribution of the disk radii $r_D$ and thicknesses $h_D$ for the disks. The form factors and structure factors were further averaged over an orientational distribution with the mean direction parallel to the fiber direction. Details of the calculations are outlined in the Supporting Information and in ref. [18]. From the orientational distribution function that describes the scattering patterns quantitatively we derive the orientational order parameter $S$, which is defined as

$$S = \frac{1}{2} \langle 3\cos^2\theta - 1 \rangle \tag{24}$$

The experimentally determined values of the order parameter can then be directly related to the flow conditions during fiber spinning. The measured and simulated SAXS patterns together with a table of fit parameters is provided in the Supporting Information.

### 3.4. Fiber Spinning and Orientational Order

In the experiments we clearly observe increasing alignment of the crystalline domains for high draw ratios $v_s/v_j$. This is
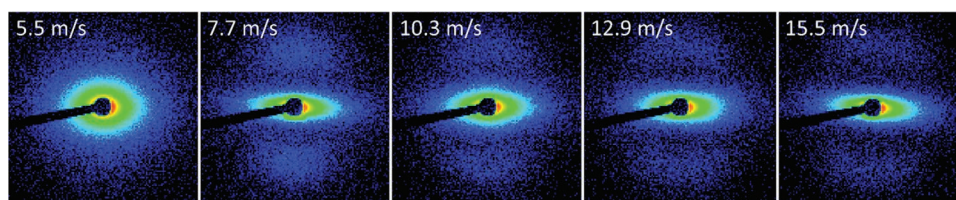
**Figure 4.** Measured SAXS patterns at increasing drawing speeds $v_s$, indicated at the upper left of each image, at a flow rate of $Q = 1.5$ mL h$^{-1}$ and a pressure difference of $\Delta p = 2.0$ bar. The increasing drawing speed leads to an increasing anisotropy in the equatorial scattering and the appearance of two broad meridional reflections due to formation of a shish–kebab crystal structure. The maximum scattering vector is $q_{max} = 1.0$ nm$^{-1}$ for all scattering patterns.

observed in the measured SAXS patterns shown in **Figure 4**, and summarized in **Table 2**, where for a constant jet velocity $v_j$ the drawing speed $v_s$ was varied. At draw ratios $v_s/v_j > 2$ values of the orientational order parameter of up to $S = 0.95$ can be achieved. This draw ratio value is in good agreement with the value of $r^* \approx 2.4$, for which a maximum elongational rate is calculated. The full set of scattering patterns together with the simulated patterns is compiled (Figures S1–S4, Supporting Information). For draw ratios slightly below 1, the orientational order is clearly decreasing, since the fiber is only stretched for $v_s > v_j$. Similarly, in **Tables 3** and **4** results are reported for constant drawing speed, where the pressure difference $\Delta p$ and thus the jet velocity $v_j$ was varied. Also, here the highest draw ratios resulted in the highest orientational order.

The nozzle–spool distance $d_s$ has a major influence on the orientation parameter $S$ and the fiber morphology, because it needs to be sufficiently long to allow solvent evaporation. Below a critical distance of 2 cm for 1.0 mL h$^{-1}$, respectively, 4 cm for 2.0, and 3.0 mL h$^{-1}$, the fibers fuse and form a network rather than individual fibers, because there is insufficient time for the solvent to evaporate from the jetted polymer solution (**Figure 5**c).[12] **Table 5** shows the orientation parameter $S$ for varied nozzle–spool distances $d_s$ at a constant draw ratio $x_s$ of 1.3. If extensional forces are absent while the fiber solidifies, the polymer chains partially lose their orientation.

Figure 5 illustrates schematically the solidification and orientation process during solvent evaporation and fiber formation. Orientation occurs in the liquid jet state indicated by the light blue cone in Figure 5. Once the fiber solidifies, it moves with the velocity of the spool $v_s$ and is no longer accelerated. At higher flow rates it takes more time for the solvent to diffuse to the surface of the bigger jets, as illustrated in Figure 5a–c. Consequently, the distance $\Delta x$ between the nozzle and the solidification point of the liquid jet increases, leading to a decreasing strain rate $\dot{\varepsilon}$. This effect can be observed for the fiber samples in Tables 2–4, when the nozzle–spool distance stays constant and the flow rate is varied. It is known that high strain rates promote the formation of microfibrils of extended chain crystals, whereas lamellar kebabs of folded-chain crystals are less developed.[20] This can be observed by a less pronounced meridional scattering for higher $v_s/v_j$ ratios in Figures S1–S3, Supporting Information.

The quantitative relation between the macroscopic flow parameters that determine the extensional rate (Equation 14) and the degree of molecular orientation of the microfibers is shown in **Figure 6**. There, the values for the order parameter $S$ determined from the scattering patterns are plotted against $\dfrac{v_s - v_j}{v_s + v_j} \times \dfrac{v_j}{Q}$ which is proportional to the elongation rate $\dot{\varepsilon}$ as given by Equation (14). We observe that despite noticeable scatter of the data, they seem to indicate a systematic relation.

**Table 2.** Orientation parameters $S$ of fiber samples at varied drawing speeds $v_s$ and flow rates $Q$ (pressure difference $\Delta p = 2.0$ bar, corresponding to jet velocity $v_j$ of 6.1 m s$^{-1}$, nozzle–spool distance $d_s = 8$ cm).

| Drawing speed $v_s$ | 5.5 m s$^{-1}$ | 7.7 m s$^{-1}$ | 10.3 m s$^{-1}$ | 12.9 m s$^{-1}$ | 15.5 m s$^{-1}$ |
|---|---|---|---|---|---|
| Draw ratio $v_s/v_j$ | 0.9 | 1.3 | 1.7 | 2.1 | 2.5 |
| 1.0 mL h$^{-1}$ | 0.79 | 0.91 | 0.92 | 0.94 | 0.93 |
| 1.5 mL h$^{-1}$ | 0.77 | 0.90 | 0.91 | 0.86 | 0.92 |
| 2.0 mL h$^{-1}$ | 0.76 | 0.90 | 0.90 | 0.88 | 0.86 |
| 2.5 mL h$^{-1}$ | 0.77 | 0.88 | 0.90 | 0.92 | 0.93 |
| 3.0 mL h$^{-1}$ | 0.76 | 0.90 | 0.89 | 0.92 | 0.94 |
| 3.5 mL h$^{-1}$ | 0.74 | 0.88 | 0.88 | 0.92 | 0.93 |
| 4.0 mL h$^{-1}$ | 0.74 | 0.89 | 0.86 | 0.93 | 0.95 |

**Table 3.** Orientation parameters $S$ of fiber samples at varied flow rates $Q$ and pressure differences $\Delta p$ (drawing speed $v_s = 7.7$ m s$^{-1}$, nozzle–spool distance $d_s = 8$ cm).

| Pressure difference $\Delta p$ | 1.0 bar | 1.5 bar | 2.0 bar | 2.5 bar |
|---|---|---|---|---|
| Jet velocity $v_j$ | 4.3 m s$^{-1}$ | 5.3 m s$^{-1}$ | 6.1 m s$^{-1}$ | 6.8 m s$^{-1}$ |
| Draw ratio $v_s/v_j$ | 1.8 | 1.5 | 1.3 | 1.1 |
| 1.0 mL h$^{-1}$ | 0.92 | 0.92 | 0.93 | 0.90 |
| 1.5 mL h$^{-1}$ | 0.90 | 0.90 | 0.86 | 0.85 |
| 2.0 mL h$^{-1}$ | 0.90 | 0.89 | 0.84 | 0.84 |
| 2.5 mL h$^{-1}$ | 0.89 | 0.86 | 0.84 | 0.84 |
| 3.0 mL h$^{-1}$ | 0.89 | 0.86 | 0.84 | 0.84 |

**Table 4.** Orientation parameters $S$ of fiber samples at varied flow rates $Q$ and pressure differences $\Delta p$ (drawing speed $v_s = 5.5$ m s$^{-1}$, nozzle–spool distance $d_s = 8$ cm).

| Pressure difference $\Delta p$ | 1.0 bar | 2.0 bar | 3.0 bar |
|---|---|---|---|
| Jet velocity $v_j$ | 4.3 m s$^{-1}$ | 6.1 m s$^{-1}$ | 7.4 m s$^{-1}$ |
| Draw ratio $v_s/v_j$ | 1.3 | 0.9 | 0.7 |
| 1.0 mL h$^{-1}$ | 0.85 | 0.82 | 0.79 |
| 2.0 mL h$^{-1}$ | 0.85 | 0.80 | 0.75 |

**ADVANCED**
**SCIENCE NEWS**
www.advancedsciencenews.com

**Macromolecular**
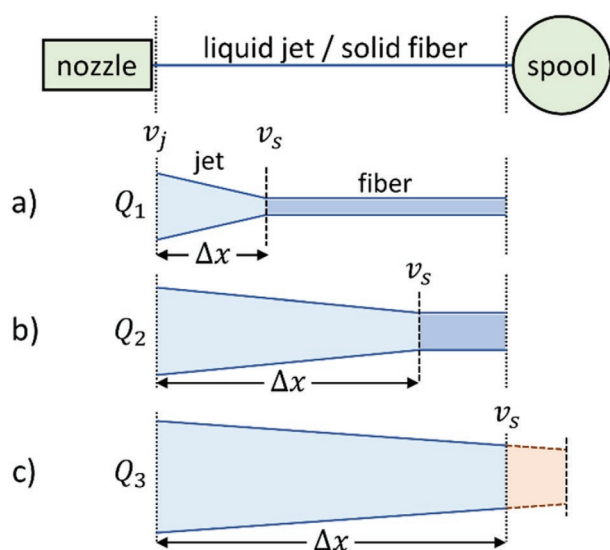**Chemistry and Physics**
www.mcp-journal.de

**Figure 5.** The theoretical progression of the diameter of the jet and subsequently the fiber is shown in this schematic diagram. The initial velocity of the jet $v_j$ and the velocity of the spool $v_s$ remain constant while the flow rate $Q$ is changed ($Q_1 < Q_2 < Q_3$) causing a shift of the solidification of the jetted polymer solution. c) The nozzle–spool distance $d_s$ is not sufficient for a complete evaporation of the solvent at flow rate $Q_3$.

This is indicated by the solid line which shows a constant base level of the orientational order, when there is no additional stretching of the fiber ($v_s < v_j$). For $v_s > v_j$, the orientational order increases until it reaches a nearly constant plateau value of S ≈ 0.94 above a value of $\frac{v_s - v_j}{v_s + v_j} \times \frac{v_j}{Q} \approx 1$. This shows that the extensional rate is the central parameter that relates the macroscopic flow parameters to the local macromolecular alignment. This furthermore shows the excellent control of the fiber properties by variation of the three flow parameters $v_s$, $v_j$, and $Q$.

So far, there have been only a few studies on the structure–property relation of THVs.[21–25] The extensional flow-induced changes of the local macromolecular orientation appears to be very similar to the well-investigated ultra-high molecular weight polyethylene,[26] polycaprolactone,[20] isotactic polypropylene,[27] and poly(vinylidene fluoride) (PV-DF).[28] Chain orientation, crystal nucleation, and growth first lead to the formation of a shish–kebab structure.[19,29,30]

### 3.5. Mechanical and Microstructural Properties during Elongation

The fluorocopolymer THV was selected as a model polymer system because it could be well spun into microfibers from an

**Table 5.** Orientation parameters $S$ of fiber samples at varied flow rates $Q$ and nozzle–spool distances $d_s$ (pressure difference $\Delta p = 2.0$ bar, drawing speed $v_s = 7.7$ m s$^{-1}$).

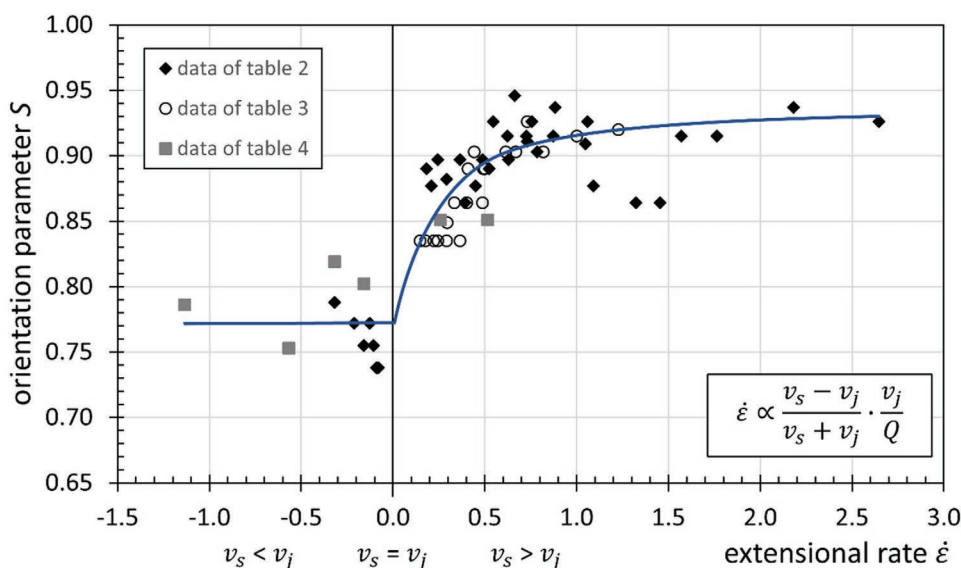| Nozzle–spool distance $d_s$ | 8 cm | 6 cm | 5 cm | 4 cm | 3 cm | 2 cm | 1 cm |
|---|---|---|---|---|---|---|---|
| 1.0 mL /h$^{-1}$ | 0.93 | 0.89 | | 0.89 | | 0.89 | 0.79 |
| 2.0 mL h$^{-1}$ | 0.86 | 0.86 | | 0.86 | 0.82 | 0.79 | |
| 3.0 mL h$^{-1}$ | 0.86 | 0.86 | 0.86 | 0.79 | 0.79 | | |



**Figure 6.** Plot of the orientational order parameter $S$ versus $\frac{v_s - v_j}{v_s + v_j} \times \frac{v_j}{Q}$, which is proportional to the elongation rate $\dot{\varepsilon}$ (Equation (14)). The values are taken from Tables 2–4. We observe a systematic increase of the orientational order parameter for $v_s > v_j$ until $\frac{v_s - v_j}{v_s + v_j} \times \frac{v_j}{Q} \approx 1$, above which a nearly constant plateau value is reached. The line is a guide to the eye.
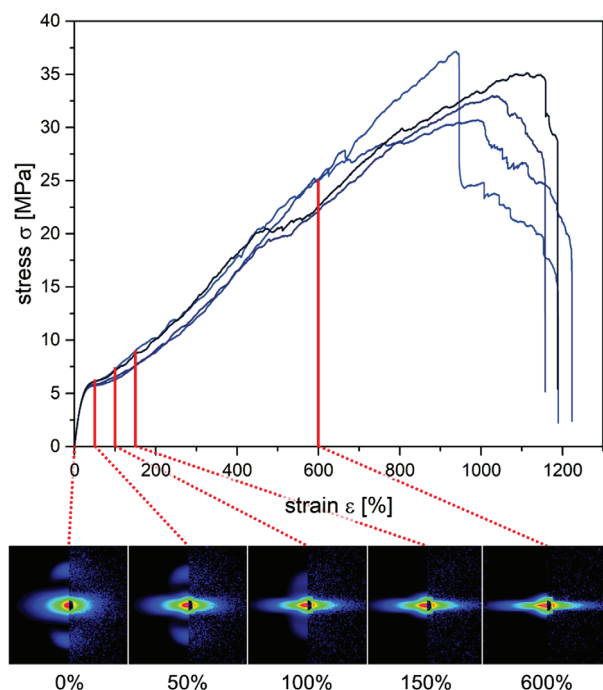
**Figure 7.** Engineering stress–strain curves for four different fiber bundles together with the SAXS patterns (right: experiment, left: simulation) measured at selected strains. All fiber bundles were produced at the same experimental conditions as described in the main text, leading to high macromolecular orientation.



**Figure 8.** Comparison of WAXS reflex at 13 nm$^{-1}$ for A) an unstretched fiber sample and B) the same sample at a strain of 500%. The reflex on the equator gets more defined. Horizontal black bars result from interstices between detector modules.

acetone solution by continuous SBS using the newly developed GDNV microfluidic nozzle device. We observed that elongation is an important factor controlling the macromolecular assembly and alignment of the emerging fiber. We therefore studied the correlation between macroscopic elongation and mechanical response to molecular scale alignment by tensile stress–strain experiments accompanied by SAXS and WAXS. For the tensile experiments, fiber bundles were produced at the optimum spinning conditions to achieve high macromolecular orientation, that is, a flow rate of $Q = 1.0$ mL h$^{-1}$, a pressure difference of $\Delta p = 2.0$ bar, a drawing speed of $v_s = 7.7$ m s$^{-1}$, a working distance of $d_s = 8$ cm, with a collection time of $t_c = 300$ s. Every fiber bundle consists of about 37 500 single fibers. The SAXS and WAXS measurements were performed with the fiber bundles fixed at selected strain values.

**Figure 7** shows the measured stress–strain curves for four different fiber bundles together with the SAXS patterns measured at selected strains. From the initial slope we obtain a value of Young's modulus of 31 MPa, which is in a typical range for rubbery materials. At strains >50% we observe a pronounced yielding and plastic deformation behavior, until for strains between 1000–1200% the fibers rupture. The maximum tensile strength is equal to 31 MPa, which is in the typical range of fluoropolymers, that is, between 10 MPa for PTFE and 46 MPa for PVDF. These and further measured mechanical properties are summarized in Table S3, Supporting Information. The mechanical properties are ideal for applications as seal tapes.
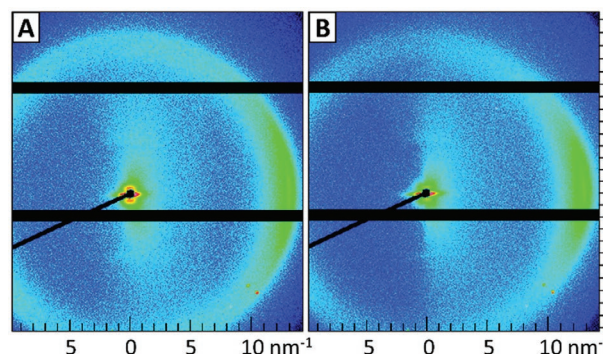
Of particular relevance are the observed microstructural changes during deformation, which can be derived from the measured 2D SAXS patterns. The measured SAXS patterns together with the simulated SAXS patterns are shown in the lower panel in Figure 7. The parameters used to simulate the SAXS patterns are summarized in Table S2, Supporting Information. Before elongation, the fibers are characterized by a weak anisotropic equatorial low-$q$ scattering, together with two Bragg peaks located on the meridian and corresponding to the disk or "kebab" lamellar spacing. Upon elongation to 50%, the intensity of the Bragg peaks decreases, while the peak position shifts to lower $q$. This indicates an increase in the disk spacing together with a disappearance of disks. This results from a transformation of the lamellae of folded chains within the disks into fibrils of extended chains.[26–28] The increase of the disk spacing is ascribed to the extension of the amorphous layers between the crystalline lamellae of the kebabs.[28]

Further elongation of the fibers to 100–150% leads to a further low-$q$ shift of the Bragg peaks, until they completely vanish. From the model calculations we conclude that the disk spacing increases from 9.8 to 12.0 nm (Table S2, Supporting Information), until the disks have completely disappeared. Concomitantly, the equatorial low-$q$ scattering becomes highly anisotropic and elongated along the equator. This can be related to a reduction of the primary fiber diameter. According to simulations of the low-$q$ scattering, the primary fiber diameter decreases from 62 to 36 nm with a concomitant increase in the order parameter from 0.84–0.99. This indicates that during elongation, the shish–kebab structure is transformed into an extended chain crystal structure, which can be plastically deformed up to high elongations.

The crystallinity in the fibers is apparent by the WAXS. **Figure 8** compares the scattering pattern of an unstretched fiber sample (A) to the same sample at a strain of 500% (B). The circular arc at $q = 13$ nm$^{-1}$ corresponds to structural features at a length scale of $d = 2\pi/q \approx 0.5$ nm, which corresponds well to the cross-sectional dimension of the fluoropolymer backbone. Upon stretching, the arc scattering intensity sharpens toward the equator, indicating an increased crystalline orientation along the fiber axis.

## 4. Conclusions

We developed a microfluidic nozzle device for µSBS to produce uniform microfibers in a highly controlled manner. The method benefits from the GDVN principle, which offers a precise control of the liquid jet diameter and velocity. We performed fiber spinning experiments together with SAXS and WAXS to relate macroscopic spinning conditions to the bulk and molecular structure of the resulting fibers. In our experiments, we demonstrate that the control provided by the GDVN-microfluidic device enables a precise control of the final fiber diameter and the fiber properties. We show that the elongational rate is the relevant parameter that relates the macroscopic flow properties to the local macromolecular structure and orientation and thus the mechanical properties of the fiber. We observe that the spinning process results in a well-defined shish–kebab crystal structure of the fiber, which evolves into an extended chain crystal structure upon plastic deformation, similar to well-investigated crystalline polymer fibers.

## Supporting Information

Supporting Information is available from the Wiley Online Library or from the author.

## Conflict of Interest

The authors declare no conflict of interest.

[1] E. S. Medeiros, G. M. Glenn, A. P. Klamczynski, W. J. Orts, L. H. C. Mattoso, *J. Appl. Polym. Sci.* **2009**, *113*, 2322.

[2] J. L. Daristotle, A. M. Behrens, A. D. Sandler, P. Kofinas, *ACS Appl. Mater. Interfaces* **2016**, *8*, 34951.

[3] J. E. Oliveira, E. A. Moraes, R. G. F. Costa, A. S. Afonso, L. H. C. Mattoso, W. J. Orts, E. S. Medeiros, *J. Appl. Polym. Sci.* **2011**, *122*, 3396.

[4] X. Zhuang, L. Shi, B. Zhang, B. Cheng, W. Kang, *Macromol. Res.* **2013**, *21*, 346.

[5] J. E. Oliveira, E. S. Medeiros, L. Cardozo, F. Voll, E. H. Madureira, L. H. C. Mattoso, O. B. G. Assis, *Mater. Sci. Eng., C* **2013**, *33*, 844.

[6] A. M. Behrens, B. J. Casey, M. J. Sikorski, K. L. Wu, W. Tutak, A. D. Sandler, P. Kofinas, *ACS Macro Lett.* **2014**, *3*, 249.

[7] J. E. Oliveira, L. H. C. Mattoso, W. J. Orts, E. S. Medeiros, *Adv. Mater. Sci. Eng.* **2013**, *2013*, 409572.

[8] M. Wojasiński, M. Pilarek, T. Ciach, *Pol. J. Chem. Technol.* **2014**, *16*, 43.

[9] J. Oliveira, G. S. Brichi, J. M. Marconcini, L. H. Capparelli Mattoso, G. M. Glenn, E. Souto Medeiros, *J. Eng. Fibers Fabr.* **2014**, *9*, 117.

[10] D. D. da Silva Parize, J. E. de Oliveira, M. M. Foschini, J. M. Marconcini, L. H. C. Mattoso, *J. Appl. Polym. Sci.* **2016**, *133*, 43379.

[11] D. D. da Silva Parize, M. M. Foschini, J. E. de Oliveira, A. P. Klamczynski, G. M. Glenn, J. M. Marconcini, L. H. C. Mattoso, *J. Mater. Sci.* **2016**, *51*, 4627.

[12] E. Hofmann, K. Krüger, C. Haynl, T. Scheibel, M. Trebbin, S. Förster, *Lab Chip* **2018**, *18*, 2225.

[13] S. Ok, B. Hartmann, H. Duran, H. Eickmeier, M. Haase, U. Scheler, M. Steinhart, *J. Polym. Sci., Part B: Polym. Phys.* **2019**, *57*, 1402.

[14] S. Ok, S. Sadaf, L. Walder, *High Perform. Polym.* **2014**, *26*, 779.

[15] A. M. Gañán-Calvo, *Phys. Rev. Lett.* **1998**, *80*, 285.

[16] D. R. Salem, *Structure Formation in Polymeric Fibers*, Hanser Gardner Publications, Cincinnati **2001**.

[17] S. Förster, L. Apostol, W. Bras, *J. Appl. Crystallogr.* **2010**, *43*, 639.

[18] S. Förster, S. Fischer, K. Zielske, C. Schellbach, M. Sztucki, P. Lindner, J. Perlich, *Adv. Colloid Interface Sci.* **2011**, *163*, 53.

[19] R. H. Somani, L. Yang, L. Zhu, B. S. Hsiao, *Polymer* **2005**, *46*, 8587.

[20] C. T. Lim, E. P. S. Tan, S. Y. Ng, *Appl. Phys. Lett.* **2008**, *92*, 141908.

[21] J. Stange, S. Wächter, H. Münstedt, H. Kaspar, *Macromolecules* **2007**, *40*, 2409.

[22] S. Begolo, G. Colas, J.-L. Viovy, L. Malaquin, *Lab Chip* **2011**, *11*, 508.

[23] H. Teng, *Appl. Sci.* **2012**, *2*, 496.

[24] S. Ebnesajjad, *Fluoroplastics: The Definitive User's Guide and Databook*, Vol. *2*, 2nd ed., Elsevier, Amsterdam **2015**.

[25] J. G. Drobny, *Technology of Fluoropolymers*, 2nd ed., CRC Press, Boca Raton, FL **2008**.

[26] M. An, H. Xu, Y. Lv, Q. Gu, F. Tian, Z. Wang, *RSC Adv.* **2016**, *6*, 51125.

[27] F. Zuo, J. K. Keum, X. Chen, B. S. Hsiao, H. Chen, S.-Y. Lai, R. Wevers, J. Li, *Polymer* **2007**, *48*, 6867.

[28] H. Guo, Y. Zhang, F. Xue, Z. Cai, Y. Shang, J. Li, Y. Chen, Z. Wu, S. Jiang, *CrystEngComm* **2013**, *15*, 1597.

[29] A. J. Pennings, J. M. A. A. Mark, H. C. Booij, *Kolloid Z. Z. Polym.* **1970**, *236*, 99.

[30] M. Cakmak, A. Teitge, H. G. Zachmann, J. L. White, *J. Polym. Sci., Part B: Polym. Phys.* **1993**, *31*, 371.